The Wide Swath Ocean Altimeter: Radar Interferometry for Global Ocean Mapping with Centimetric Accuracy[1,2]

Brian D. Pollard, Ernesto Rodriguez, Louise Veilleux, Torry Akins, Paula Brown, Amirit Kitiyakara, and Mark Zawadski
Jet Propulsion Laboratory
California Institute of Technology
4800 Oak Grove Drive
Pasadena, CA 91109
818.354.7718
brian.pollard@jpl.nasa.gov

Somsak Datthanasombat and Aluizio Prata, Jr.
University of Southern California
Los Angeles, CA 90089-0271

Abstract— The recent Shuttle Radar Topography Mission (SRTM) has demonstrated the capability for global interferometric topographic mapping with meter level accuracy and 30 meter spatial resolution. The next challenge in radar interferometry is the measurement of ocean topography: the global characterization of ocean mesoscale eddies requires global coverage every 10 days, with centimetric height accuracy, and a spatial resolution of 10-20 km.

We have developed an instrument concept that combines a conventional nadir altimeter with a radar interferometer to meet the above requirements. In this paper, we describe the overall mission concept and the interferometric radar design. We also describe several new technology developments that facilitate the inclusion of this instrument on a small, inexpensive spacecraft bus. Those include ultra-light, deployable reflectarray antennas for the radar interferometer; a novel five frequency feed horn for the radiometer and altimeter; a lightweight, low power integrated three frequency radiometer; and a field programmable gate array-based onboard data processor. Finally, we discuss recent algorithm developments for the onboard date processing, and present the expected instrument performance improvements over previously reported results.

TABLE OF CONTENTS

1. INTRODUCTION
2. MISSION CONCEPT
3. INSTRUMENT DESIGN
4. ONBOARD ALGORITHM IMPROVEMENTS
5. SUMMARY

1. INTRODUCTION

The TOPEX/Poseidon (T/P) mission demonstrated clearly the possibility of using nadir altimetry to obtain centimetric accuracy in measuring ocean topography. However, the temporal and spatial sampling characteristics of nadir-looking altimeters like T/P are such that the full spatial spectrum of oceanic variability cannot be observed: the 10 day repeat period required to avoid tidal aliasing means that T/P has equatorial gaps of approximately 300 km, much larger than a typical mesoscale ocean feature.

In [1], Rodriguez et al. propose a new measurement concept, a Wide Swath Ocean Altimeter (WSOA), that allows nearly complete global coverage of the ocean spatial spectrum while maintaining the 10 day repeat orbit of T/P, all from a single platform. The WSOA mission concept adds an across-track interferometer to a standard, T/P-like altimeter suite to obtain a swath of 200km. This interferometer, similar in concept to the recent Shuttle Radar Topography Mission (SRTM), uses a novel self calibration technique to eliminate the stringent requirements on baseline metrology, and to allow for centimetric height accuracy.

While the mission concept is introduced in [1], the primary focus of that paper is to detail the cross-over calibration algorithm that makes this interferometric measurement possible, with only a cursory discussion of the instrument design. Our purpose here is to supplement [1] with a full description of the WSOA interferometric radar design, with a special focus on the new technology developments that have been required to accommodate the instrument on a small spacecraft bus. Those include ultra-light, deployable reflectarray antennas for the radar interferometer; a novel five frequency feed horn for the radiometer and altimeter; a lightweight, low power integrated three frequency radiometer; and a field programmable gate array (FPGA) based onboard data processor.

[1] 0-7803-7231-X/01/$10.00/© 2002 IEEE
[2] IEEEAC paper #008, Updated Sept 24, 2001

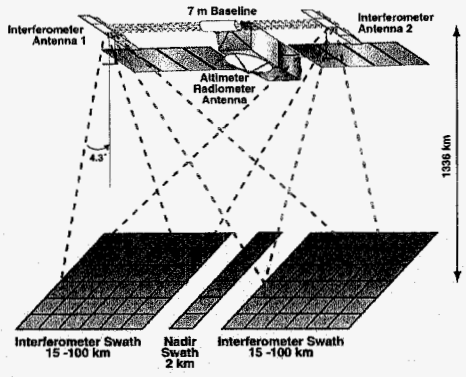

Figure 1: The WSOA mission concept.

In addition to the instrument design and technology, we also present revisions to the onboard data processing algorithm presented in [1]. We show that minor modifications can improve the registration and geometric decorrelations of the radar interferometer, and lead to substantial performance improvements.

The plan of this paper is as follows. In the following section, we review the overall mission concept, present the expected instrument coverage, and describe the basic system parameters. In Section 3, we discuss the instrument design in more detail, with subsections devoted to the radar interferometer antenna, RF electronics, and data handling electronics, mentioning, where appropriate, the related technology developments. We also review the three frequency radiometer design, including the recent five frequency feed, noise source, and monolithic microwave integrated circuit (MMIC) receiver developments. We then present, in Section 4, the modifications to the onboard data algorithms, and the resulting performance improvements. We conclude with a brief summary in Section 5.

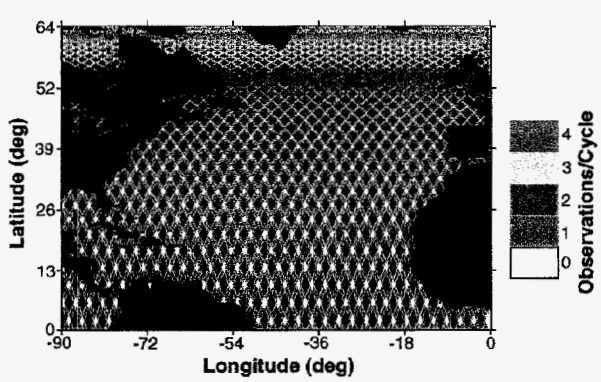

Figure 2: Example WSOA coverage. The color table represents the number of observations from WSOA in any 0.1 degree cell in a 10 day cycle.

Table 1: The key WSOA interferometric radar parameters.

Parameter	Unit	Value
Center Frequency	GHz	13.28
Bandwidth	MHz	20
Pulse Length	us	45-90
Pulse Repetition Frequency	Hz	1036
Peak Transmit Power	W	120
Antenna Width	m	0.3
Antenna Length	m	2.5
Antenna Boresight	deg	3.3
Baseline Length	m	6.4

2. Mission Concept

Figure 1 presents the WSOA mission concept. A standard, T/P-like altimeter and radiometer suite is supplemented by a Ku-band across track radar interferometer. The interferometric baseline is created by a deployable 6 to 7 meter boom, with deployable Ku-band reflectarray antennas at each end. The interferometer is a dual-swath system, alternatively illuminating the left and right swaths. Each swath is 85 km in extent, starting at 15 km from the nadir track and extending to 100 km from the nadir track, creating an overall swath of 200 km. The pixel resolution of the interferometric system is 14 km by 14 km. The key radar parameters are given in Table 1.

As discussed in [1], in a T/P like orbit (1336 km, 66 degree inclination, 10 day repeat) the WSOA mission obtains nearly complete global coverage in a 10 day cycle. Figure 2 shows an example coverage map, where the color table represents the number of times a given 0.1 degree cell is sampled in a 10 day cycle. Such coverage would allow for study of mesoscale eddies, which typically have spatial scales of 100 km, and temporal scales of 30 days.

3. Instrument Design

Figure 3 shows another view of the WSOA instrument, with the locations of various components indicated. The majority of the electronics are mounted within the spacecraft bus, with the notable exception of the interferometer transmitters, and a portion of the receivers (the low noise amplifiers, in particular). In this section, we describe a number of the subsystems shown in Figure 3 in more detail. We have focused our efforts to date on the interferometric radar and the three frequency radiometer portions of the WSOA suite, and the details below reflect that focus.

Reflectarray Antenna Design

Functionally, the interferometer antennas must illuminate alternate sides of the swath on successive pulses, while

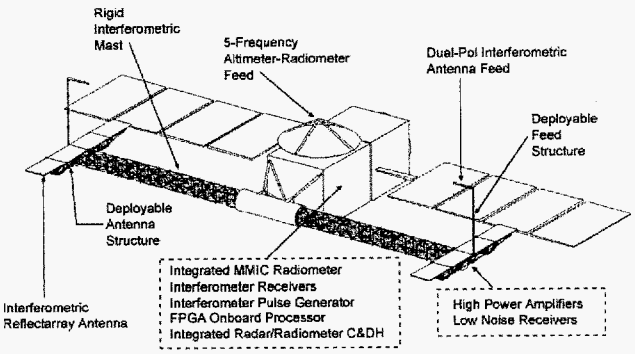

Figure 3: A closer view of the WSOA instrument concept. The locations of the various subassemblies are shown.

minimizing the coupling between the two swaths. Structurally, the antennas must be low mass and stow to within a relatively small volume, while maintaining stringent stability requirements. To meet those requirements we have developed a reflectarray antenna with a low mass, ultra-stable antenna support structure.

The guiding principle of reflectarrays is quite simple: etched elements on the panel surfaces provide the phase change required to emulate a parabolic reflector. Each of the WSOA reflectarrays consists of five coplanar 45 cm by 35 cm panels of elements, resulting in an aperture size of 225 cm by 35 cm. Our present design uses panels made of Ultralam® 1217 from Rogers Corporation (ε_r of 2.2), although an air dielectric design is also under consideration due to mass and thermal concerns.

The element design is crucial with reflectarrays, particularly at and above Ku-band, as manufacturing and etching errors can severely impact the performance. Our recent studies [2] have shown that a spiral patch, tunable by changing the outer arm lengths, is more tolerant of such errors. A sample patch is shown in Figure 4.

Our requirement of minimal coupling between alternate swaths has led us to use a dual-polarization antenna: alternate linear polarizations are used for each swath. One area of complication with this choice is with the feed, which must now be dual polarization.

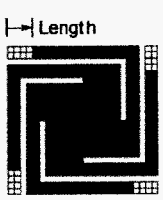

Figure 4: The spiral patch geometry employed by the WSOA reflectarrays.

In order to minimize ohmic losses, a slotted waveguide array has been selected for each feed. The illumination pattern requires a 10 dB taper to the edges of the reflectarray, corresponding to 10 dB beamwidths of approximately 90° in the long dimension of the reflectarray, and 19° in the short dimension. 2x7 element array geometries have been selected to meet this requirement for both polarizations.

The feed for the horizontal polarization consists of two resonant 1x7 narrow-wall slotted waveguide arrays placed side-by-side. To reduce cross-polarized radiation in the broadside direction, the two arrays are mirror images of one other and therefore require a 180° phase difference between their feed points. A folded H-plane magic tee is being considered to provide the required 3 dB power split and 180° phase difference between the two 1x7 arrays. Standard WR-62 waveguide dimensions were selected for this feed. The slots are separated by a half guide wavelength and introduce a shunt admittance into the waveguide transmission line circuit model. For a good match at the input to each 1x7 array, the normalized slot admittance was designed to be 1/7+j0, including the effects of mutual coupling.

The feed for the vertical polarization consists of a resonant 2x7 broad-wall slotted waveguide array. A wide waveguide geometry permits the structure to be fed with a TE_{20} waveguide mode, which provides the 180° phase shift necessary between each half of the waveguide to generate

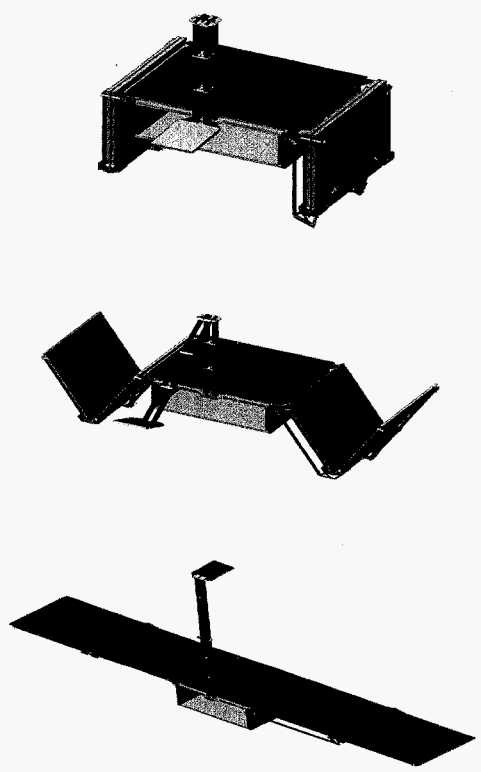

Figure 5: The WSOA interferometric antenna deployment sequence.

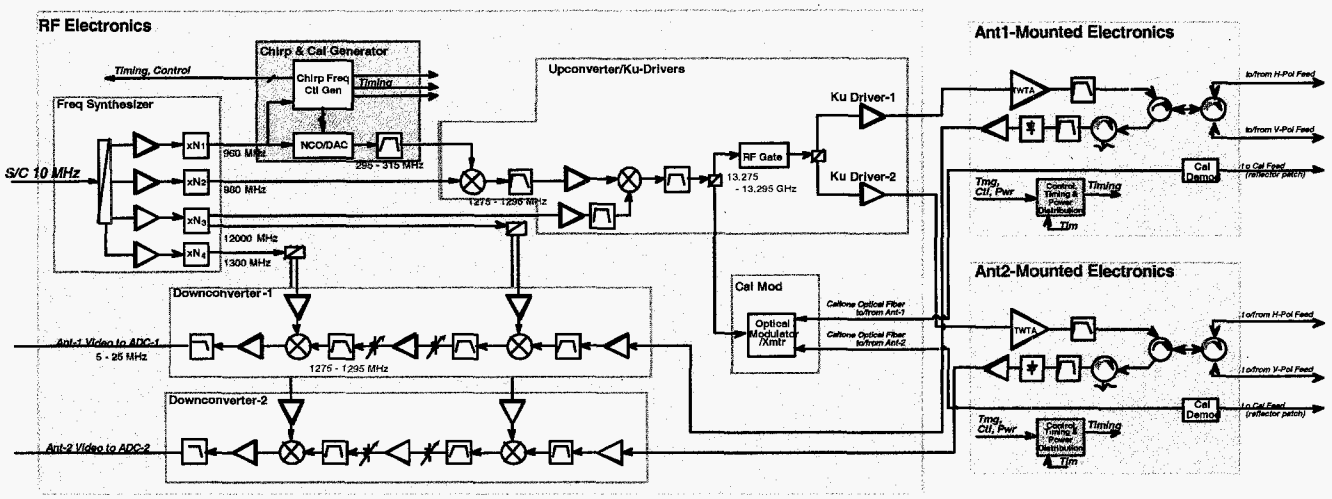

Figure 6: The WSOA interferometer RF electronics block diagram. The bus-mounted electronics are at left, while the tip-mounted electronics are at right.

the required beam. (This approach is similar to two adjacent 1x7 arrays sharing a common narrow wall with each waveguide fed 180° out-of-phase. The advantage of removing the common wall is a reduction in the mass of the antenna). The waveguide is ridged in order to shorten the guide wavelength and provide the required array spacing for the specified beamwidth.

Turning from the electrical portion of the interferometer antenna design to the structural, we note that the dominant source of systematic error (accuracy) in the WSOA interferometer is the antenna position knowledge and phase center stability. As an example, in order to obtain centimetric accuracy, the relative phase center between the two antennas must vary by less than 0.1 degrees. Thus, the structural stability of the antennas is of prime importance.

With the assistance of the AEC-Able Corporation, we have designed, developed, and tested a brassboard deployable antenna and feed support structure. This structure is quite light, with an expected mass of 2.4 kg for the flight unit, and extremely repeatable and stable: repeatability tests have shown less than 0.15 mm variations across all dimensions, and the predicted stability results keep the phase centers to within our stringent requirements. Figure 5 shows the deployment sequence of the support structures.

Radio Frequency Electronics

The signal generation, amplification, reception, and downconversion are all functions of the RF Electronics portion of the WSOA interferometer. Figure 6 presents the design of this subsystem, which includes assemblies both within the spacecraft bus, and behind the interferometer antennas, at the mast tips.

In this subsection, we briefly step through the subassemblies in Fig. 6. At the left of the figure, the frequency synthesizer uses a 10 MHz spacecraft frequency reference to generate coherently the frequencies required for interferometer signal generation, upconversion, and downconversion The 960 MHz output of the synthesizer is passed to the Chirp and Cal-tone Generator, which digitally produces a 20 MHz linear chirp. The output of the Chirp Generator is then upconverted to L-band (1.285 GHz) and passed into the Upconverter and Driver subassembly, where it is mixed up to Ku-band (13.285 GHz) and amplified to drive the tip-mounted power amplifier. After passing up the mast cabling, the signal is amplified to full power by a traveling wave tube amplifier (TWTA), and routed to the appropriate antenna feed for transmission.

Upon reception, each signal is amplified by a low noise amplifier, mounted at the tip in order to improve the system noise figure. After passing down the mast cabling, each received signal is downconverted to a video signal (15 MHz) and sent to the Data Handling Unit.

The critical challenge of the RF design is the phase tracking of the two receiver chains. Careful thermal packaging of the bus-mounted downconverter assemblies as well as minimization of thermal coefficient for the antenna-mounted receive components is planned to minimize channel-to-channel phase differences. A calibration tone routed through each receiver, using an optical conversion scheme to distribute the tones with equal phases at their injection points, is also planned to allow for removing receiver phase errors in the processed data.

Three Frequency Radiometer

A further part of the WSOA instrument concept, the three frequency radiometer measures single polarization, radiometric brightness temperature in a nadir beam co-aligned with that of the nadir-looking altimeter. The three channels include a 21.0 GHz channel, the primary water vapor sensor, an 18.7 GHz channel to estimate ocean surface components in the observed brightness temperature, and a

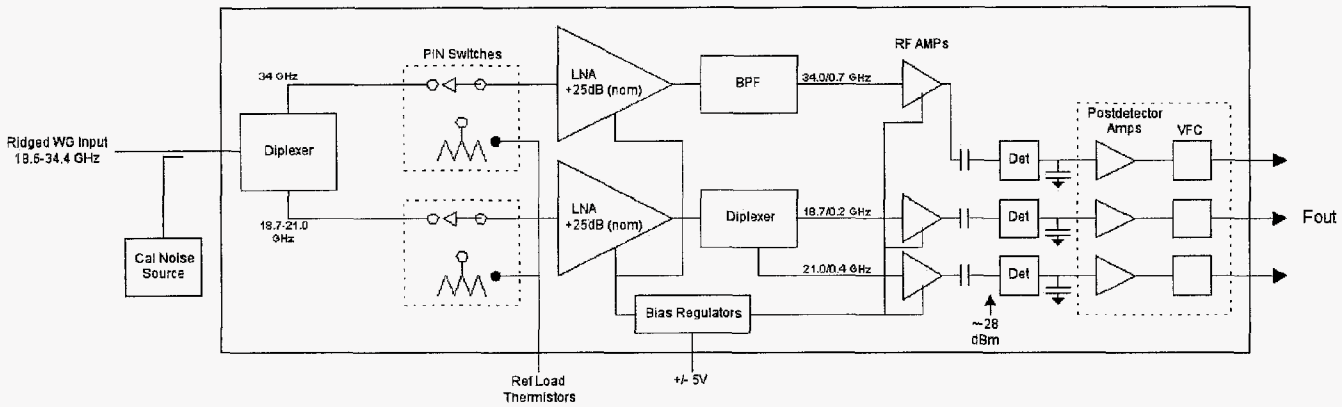

Figure 7: The Jason-2 Microwave Radiometer receiver block diagram. The three frequencies have been integrated into a single, MMIC receiver.

34.0 GHz channel to estimate cloud liquid. An antenna pattern correction is applied to the resulting measurements to correct for brightness temperature contributions from outside the main beam, and a retrieval algorithm using empirically derived coefficients yields the wet path delay estimate for altimeter range correction.

Figure 7 shows a block diagram of the radiometer receiver. The broadband, double-ridged waveguide input port supports all three channels and provides a simple, single-flange radiometer to feedhorn interface. The calibration noise source provides gain calibration using redundant, bias-switched noise diodes in a hybrid circuit, integrated with a broadband, ridged waveguide directional coupler that enables gain calibration directly through the input signal path. To supplement the noise diodes, the absolute calibration accuracy will be assessed throughout the mission using analyses of the coldest observed brightness temperatures corresponding to clear sky, calm ocean conditions, and by intercomparisons with upward looking, ground-based water-vapor radiometers.

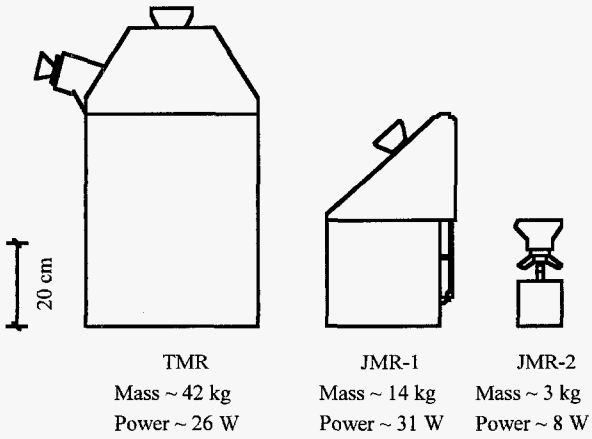

Figure 8: Size, mass, and power comparisons of the next generation radiometer (JMR-2) compared to the units aboard TOPEX (TMR) and Jason-1 (JMR-1).

To obtain optimum noise figure tuning from the receiver front-end components, the input signal is channelized into two bands using a waveguide frequency diplexer. Waveguide to microstrip transitions follow the diplexer to allow the rest of the receiver to be realized in a miniaturized, planar architecture. GaAs MMIC PIN diode switches provide "Dicke" switching between the input signal and an internal reference load, which reduces the effects of low-frequency amplifier gain fluctuations. After several stages of amplification by GaAs MMIC's, and separation of the 18.6 and 21.0 GHz bands by a planar diplexer, the signals are detected using a tunnel diode, square-law detector. The detector signals are amplified and converted to a pulse train using voltage to frequency converters (VFC). The VFC signals are output to gated frequency counters in a separate data acquisition module, which provides integrating analog to digital conversion of the radiometer measurements.

The single, three channel MMIC receiver allows us to make substantial mass, power, and volume savings over previous generation three frequency radiometers, such as the TOPEX microwave radiometer (TMR), or the Jason-1 Microwave Radiometer (JMR-1). Figure 7 shows a comparison with our present design, here labeled as the Jason-2 Microwave Radiometer (JMR-2), with the TMR and JMR-1 units, while Figure 8 shows a photo of the brassboard JMR-2 receiver.

We have also developed, with the Microwave Engineering Corporation (MEC), a novel five frequency feedhorn that enables a single antenna system to be shared between the altimeter and the radiometer. This elimination of the dedicated radiometer feedhorn and reflector simplifies the spacecraft configuration and increases the options in accommodating the proposed WSOA instrument on a small spacecraft. This feedhorn supports both the C and Ku band altimeters as well as the 18.7, 21.0, 34.0 GHz radiometer channels. Figure 9 shows a photo of the multi-octave feedhorn brassboard.

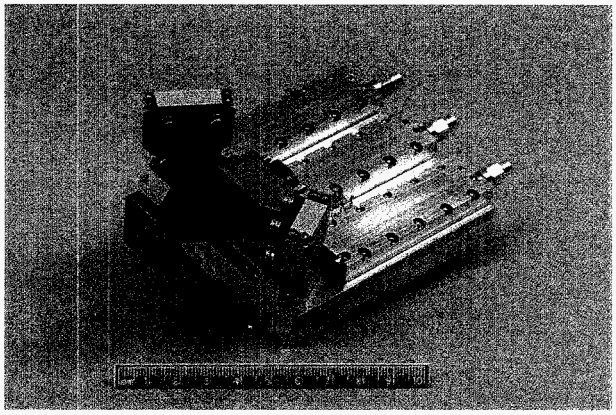

Figure 9: Three frequency radiometer receiver brassboard.

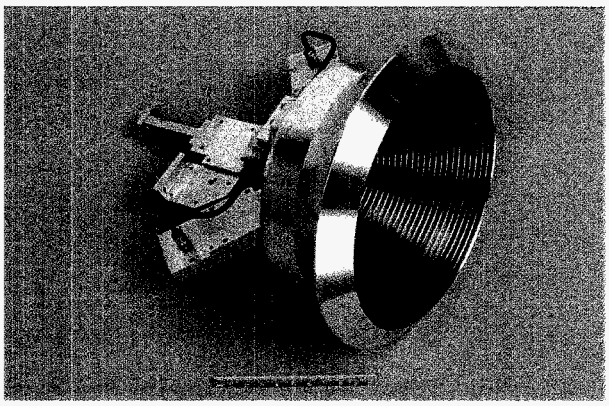

Figure 10: The multi-octave feedhorn brassboard.

Data Handling and Control Electronics

The data from both the radiometer and the interferometer is handled by a central data handling unit (DHU), which also is responsible for controlling both instruments. A block diagram of this unit is shown in Figure 10. Three modules are contained in this unit: a central VME cage, housing a number of sub-modules, and the two outboard electronics units, located behind each antenna, at the mast tips. Also shown in Figure 10 are the subsystems that communicate with the data handling unit. Among those are RF electronics, including the digital chirp generator (DCG), any mast and antenna deployment actuators, and the radiometer. The DHU must also provide interfaces to and from the nadir altimeter and the spacecraft.

The flight computer, housed in the VME cage, commands and receives telemetry and data from the sub-modules. We have chosen the General Dynamic GDIS-6U-VME-4603RT for this function. Based on four Power PC 603e processors running in lockstep, this flight computer has a very low probability of upset due to radiation. Also included is a MIL-STD-1553 interface, five serial ports, and onboard flash memory. All of these features are used in our present design.

The power distribution unit (PDU), also housed in the VME cage, regulates the spacecrafts +28V to provide power to the entire radar/radiometer system. The flight computer receives power through the VME backplane, while the rest of the modules receive power through external connections in order to accommodate different power-on modes. Presently a mere three modes are envisioned: Off, Standby, and On.

The radar timing unit (RTU) implements all the timing and control signal for the instrument. It creates the triggers to the digital chirp generator and the real-time processors., and controls the gain settings in the RF electronics. All the controls parameters of the RTU are loaded through the VME interface. The flight computer also loads the time tag into the RTUs time counter preload register. The one pulse per second from the spacecraft initiates the transfers of this register into the time counter.

The Analog to Digital Converter (ADC) sub-module contains 2 A/D converters, each sampling at 60 MHz. The four most significant bits of this data is routed to the two real-time processor boards.

The real time processor prototype was developed around the Xilinx Virtex Field Programmable Gate Arrays (FPGA). Each device contains 1 million static random access memory (SRAM) based programmable gates. The prototype board is shown in Figure 11. All of the components, including the FPGAs, have a space qualified equivalent part. The density and speed of the Xilinx FPGAs allow the entire onboard processor to be placed on a single VME card, while the reconfigurablity of the device allows for the algorithm to change during the development and after launch.

The nominal (see Section 4) onboard processing algorithm is shown in Figure 12. 8192 samples from each channel are digitally down-converted, filtered, and decimated by two. Each channels 4096 complex samples are stored in a buffer. Each channel is then passed though the pulse compressor. The pulse compressor is implemented by performing a 4096-point fast Fourier transform (FFT), then multiplying by the reference function, and transforming back to the time domain with a 4096-point inverse-FFT. After the first channel is pulse compressed it is stored in external memory until the second channel is pulse compressed, then the complex conjugate of the first and second channel is calculated. Along track averaging is performed on multiple range lines and the result is moved into the output buffer.

The last submodule in the VME chassis is the actuator control unit (ACU). This module interfaces with the mast actuator and the antenna deployment mechanism. Commands are sent through the VME interface to control

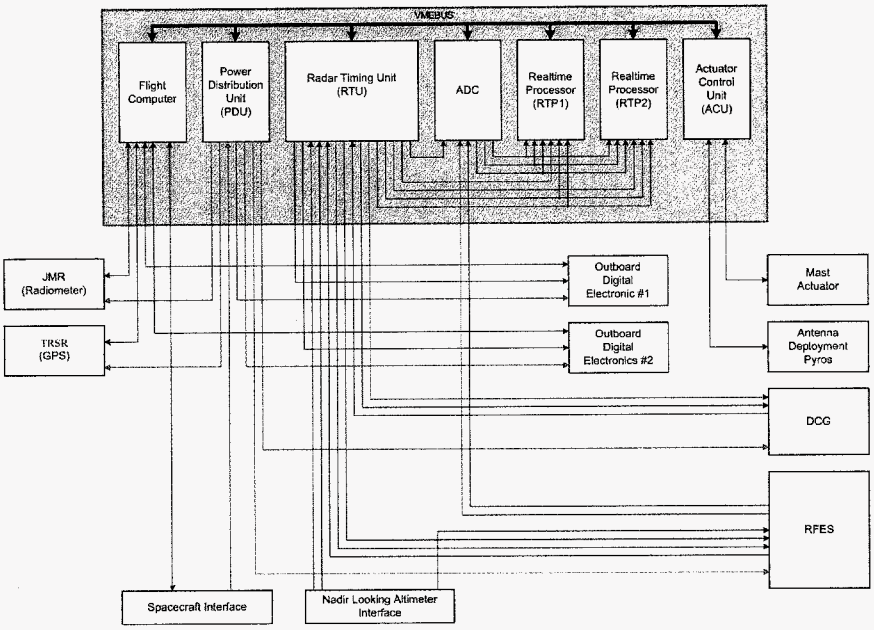

Figure 11: The WSOA interferometer data handling unit block diagram.

the deployment of the mast and the antenna. Telemetry from this module allows the flight computer to determine the current draw of the mast actuator.

The last two modules in the digital subsystem are the digital outboard electronics (OBE). There is one in each mast tip structure. These modules receive commands and send telemetry through a serial interface with the flight computer. All the telemetry from the tip structure is gathered by the OBE. Serial commands include power and heater control.

ONBOARD ALGORITHM IMPROVEMENTS

The algorithms used both to form the interferometric height measurement are described above and in more detail in [1]. In this section, we describe a number of modifications to those algorithms that significantly improve performance.

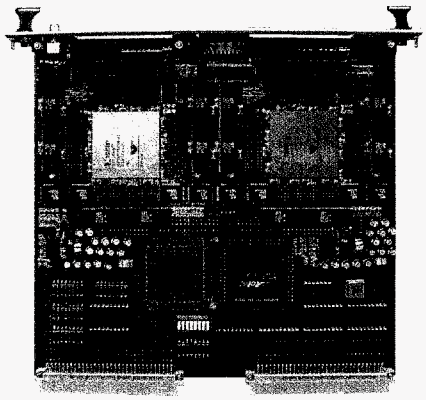

Figure 12: The WSOA onboard processor breadboard unit.

To begin, we note that the signals received by the two interferometer antennas are not perfectly correlated. The sources of decorrelation can be classified as follows: thermal noise; geometric decorrelation, which occurs because, at boresight, the surface will speckle in a slightly different fashion for each receiver; angular decorrelation, which occurs because iso-phase lines are not aligned with iso-range lines; and misregistration, which occurs when the returns are not completely aligned. The magnitude of these decorrelations are quantified for the simple design presented in [1].

After some additional thought, we have realized that for a minor computational penalty on the on-board processor, it is possible to eliminate two of the sources of decorrelation: the geometric and misregistration correlations.

In addition to improving phase noise, it is possible to reduce height noise by making the measured interferometric phase difference more sensitive to height variations. This can be accomplished by extending the interferometric baseline. However, it can also be accomplished by transmitting from both interferometric antennas, as described below.

The following subsections describe how these sources of error can be incorporated into the WSOA design, the penalties incurred in doing so, and the gains in performance.

Improving Channel Co-Registration

Due to the fact that the two interferometric receivers are separated by the interferometric baseline, signals from the

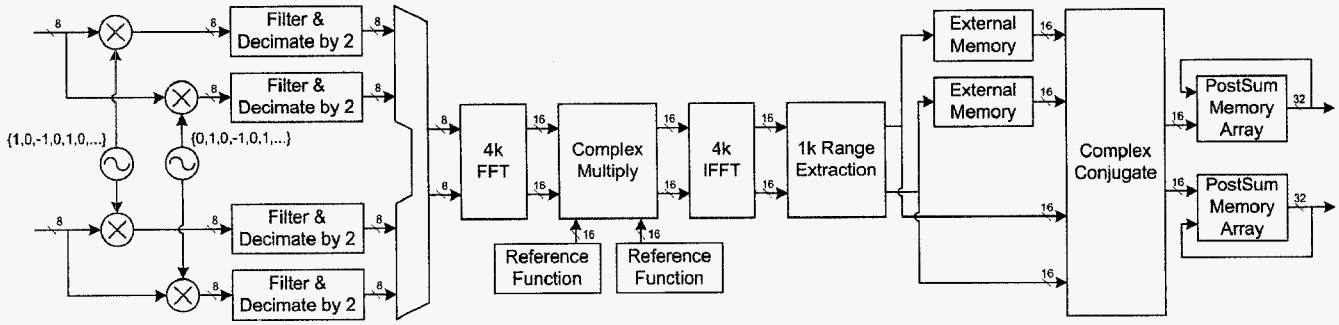

Figure 13: The nominal onboard processor algorithm.

same point on the ground will arrive at different times at the receivers. It is possible to add a single delay between the channels so that the signals are co-registered for a given incidence angle. However, residual misregistration will still occur away from the selected direction.

In order to perform channel registration, conventional synthetic aperture radars (SAR) use an interpolation algorithm using a finite interpolation kernel. However, in order to preserve phase accuracy, the kernel length is not small, and the procedure is computationally expensive.

The WSOA is a real aperture radar, and we show in Appendix A that in this case the interpolation of the two channels can be performed add a small computational cost using the chirp-z or chirp scaling algorithm [3,4]. In contrast to conventional SARs, the co-registration during range compression does not disturb subsequent synthetic aperture image formation.

As shown in Appendix A, the computational cost of using chirp-scaling for co-registration is small and can be easily incorporated into the current WSOA design.

The Wavenumber Shift and Geometric Decorrelation

The source of geometric decorrelation is the fact that the interferometric phase is not constant for all the scatterers within a given resolution cell. This variation in the interferometric phase causes the total interferometric contribution from that cell to add slightly incoherently, thus reducing the signal correlation.

Gatelli et al. [5] note the following: suppose that one is dealing with monochromatic signals, and chooses the wavelengths of the two channels to be such that the projected wavevectors on the ground are identical for both channels. In this case, the interferometric phase would be constant for all scatterers in the resolution cell, and the returns would add coherently.

When dealing with a finite bandwidth signal, things are a bit more complicated, but Gatelli et al. [1994] provide a solution: take the signal from both channels and shift the spectra in such a way that the appropriate wavelengths are multiplied together so that the phase variation over the resolution cell is canceled. This spectral shift means that noise is now brought into the processing bandwidth. In order to remove this additional noise, Gatelli et al. propose to use a low-pass filter so that only the parts of the spectra which overlap contribute to the interferometric return. The penalty for this low-pass filter is a loss in resolution, but this loss is usually small and acceptable.

The wave-number shift proposed by Gatelli et al. [1994] applies to SARs, where the angular variation of the resolution cell in the azimuth direction is very small, so that iso-range and iso-phase lines can be considered to be aligned. However, this situation no longer applies for the WSOA: since it is a real aperture system, significant deviations can occur between these two sets of lines. Viewed in another way, this is equivalent to saying in the monochromatic case that two wavelengths can be found to cancel the interferometric phase for one given azimuth direction, but not for all.

In Appendix B, we show the effects of implementing the wave-number shift for WSOA: the geometric correlation term can be made to disappear, but the angular correlation term remains. Nevertheless, the performance gains are still significant enough to warrant the inclusion of this algorithm in the WSOA on-board operation.

The operations involved in implementing the wave-number shift consist of shifting the spectrum of the two signals after range compression by multiplying both with a phase ramp in time, followed by FIR filtering of the signals. The spectral shift can be combined with the last step of the chirp-scaling algorithm, which also involves multiplying each signal sample with a complex number, so that no computational penalty is involved. There is a computational penalty involved in FIR filtering the signals, but for small filter kernels, as will be the case for WSOA, the number of computations is small compared to performing the range compression.

A study of the modifications required show that the on-board processor already prototyped for WSOA is capable of accommodating both chirp scaling and the wavenumber shift.

Ping-pong Interferometric Operation

If one transmit out of one antenna and receives in both, the interferometric phase difference will be given by

$$\phi = 2kr_1 - k(r_1 + r_2) = k(r_1 - r_2) \approx kB\sin\theta$$

However, if it were possible to transmit and receive out of one antenna, followed by transmitting and receiving out of the other one (which is called ping-pong mode in conventional interferometry), the interferometric phase would be

$$\phi = 2kr_1 - 2kr_2 \approx 2kB\sin\theta.$$

In other words, operating in ping-pong mode results in obtaining an effective baseline which is twice as long as the physical baseline.

One usually thinks of implementing ping-pong mode by alternating the antenna used for transmit with every pulse. However, this simple approach does not work for WSOA: it is well known that for distributed scatterers, such as the ocean surface, pulses which are separated by more than one-half an antenna length are not correlated. Therefore, in order to implement ping-pong mode one must transmit bursts of pairs of pulses, with the pulse separation being such that the two pulses are correlated and fit in the same return window.

In order to do this and retain constant average power, the pulse length of the two pulses must be halved, leading to a decrease in the signal-to-noise ratio (SNR). However, it can be shown that the height noise is proportional to the square root of the SNR, while the proportional to the inverse baseline length so that roughly a factor of 1.4 (square root of 2) performance gain can be achieved.

An additional concern when using close pulse pairs for ping-pong mode is that the range ambiguities will increase, degrading performance. Similarly, one must be careful to chose the pulse repetition frequency and the pulse spacing so that both returns fit with the return window without interference, and there is no interference with the nadir altimeter.

A detailed calculation shows that for the proposed WSOA system, a pulse spacing can be found such that the range ambiguities from the second pulse does not significantly increase the range ambiguity level: in practice, the range ambiguity is always dominated by the 0th, opposite side ambiguity. Further reduction of ambiguity contamination can be achieved by using opposite direction chirps for each pulse. Similarly, a PRF can be found such that ping-pong operation can occur simultaneously with the nadir altimeter.

The real cost of using ping-pong mode is the increase load on the on-board processor. One can show that a pulse length can be used such that half the range samples are required for the compression of each channel. However, using ping-pong mode introduces an additional calibration error on the transmit channel which canceled out in "standard" operation. This additional transmit phase imbalance can be calibrated using the null-baseline interferogram, but at the cost of roughly doubling the required number of range compressions, increasing by a factor of 2 the processor power requirements.

Performance Improvements

We have taken into account the changes proposed above and calculated the expected performance for instantaneous mapping for an interferometric baseline of 6.4 m, assuming a single-transmit chirp length of 90 μsec, and a ping-pong chirp length of 45 μsec. The ocean σ_0 was assumed to be in the 95% percentile (only 5% darker ocean conditions), in order to be conservative. The results for standard operation with and without chirp-scaling and wavenumber-shifts are presented in Table 2.

Notice that a performance gain from 30% to 50% can be achieved by using these improved processing and operating techniques. It should also be emphasized that these results are for the instantaneous performance of the interferometer. Due to the wide-swath capabilities, all imaged points will be revisited from 2 to 4 times within 10 days (see Fig. 2), so that additional gains in performance can be expected. Using optimal interpolation or simple averaging can also significantly reduce the error estimated over a repeat cycle.

Table 2: Height errors from the WSOA interferometer, before and after onboard processing improvements.

Cell Center (km)	Height Error w/o Proc Improve. (cm)	Height Error w/ Proc Improve. (cm)
22.1	5.2	4.1
36.4	4.7	3.3
50.7	4.5	2.9
65.0	4.6	2.8
79.2	5.2	3.1
93.5	6.5	3.9

SUMMARY

In this paper, we have discussed the WSOA instrument concept, and some of the design details of the interferometric radar and three frequency radiometer. We have also shown three methods of performance improvement that decrease the expected height error the interferometer by 30-50%.

APPENDIX A

If uniform and identical sampling is used for both radar channels, the imaged pixels on the ground will fail to line up exactly due to the slightly different viewing geometry for each channel.

The range difference between the channels is two given by

$$\Delta r \approx B\sin\theta_0 + B\frac{\cos\theta_0}{\tan\theta_0}\frac{\delta r}{r_0}$$

where B is the interferometric baseline, θ_0 is the angle to a reference point, r_0 is the range to that point, and δr is the range relative to the reference range, and the expansion has been taken to the center of the swath.

Assuming that the first channel is sampled as $r_1 = r_0 + \delta r$, the second channel must be sampled at the ranges

$$r_2 = r_0 + B\sin\theta_0 + (1+\zeta)\delta r$$

where

$$\zeta = \frac{B}{r_0}\frac{\cos\theta_0}{\tan\theta_0}$$

Assuming that constant timing differences are taken care of by suitably choosing the range compression function, the co-registration problem is reduced to sampling the second channel at $(1+\zeta)\delta r$ if the first channel is sampled at δr. This can be accomplished by using the chirp-scaling algorithm [3,4]. The details are given in the following paragraphs.

Assume the transmit signal is given by

$$S(t) = A(t)e^{i\alpha t^2}e^{i\varpi_0 t}$$

In terms of the system bandwidth Δf and the chirp duration T, $\alpha=\Delta f/(2T)$. The received signal from a point target after down-conversion is given by (after removing the shift to the center pixel)

$$S(t) = A(t-\tau_0)e^{i\alpha(t-\tau_0)^2}e^{-2ik_0 r_2}$$

where

$$\tau_0 = \frac{2}{c}(r_2 - r_0 - B\sin\theta_0),$$

k_0 is the center frequency wavenumber, r_2 is the second channel range to the point target.

We proceed to apply the chirp scaling algorithm by multiplying the signal prior to range compression by the quadratic phase factor $\exp[i\beta t^2]$, where $\beta=\alpha\zeta$.. Range compression and resampling are achieved by convolving the signal with the reference function $\exp[-I(\alpha+\beta)t^2]$, so that the range compressed signal can be written as

$$S(t) = e^{-2ik_0 r_2}\int A(\tau-\tau_0)e^{i\alpha(\tau-\tau_0)^2}e^{i\beta\tau^2}e^{-i(\alpha+\beta)(\tau-t)^2}d\tau$$

Defining the point target response as

$$\chi(t) = \int A(\eta)e^{2i\alpha\eta t}d\eta$$

the return signal can be written after some rearrangement of terms as

$$S(t) = e^{-2ik_0 r_2}e^{-i\alpha(1+\zeta)t^2}e^{i\alpha\tau_0^2}e^{2i\alpha\nu}\chi(\nu) \qquad \text{(A1)}$$

where ν is defined as

$$\nu = (1+\zeta)t - \tau_0.$$

If $\beta=0$ (i.e., no chirp scaling), the result at would be

$$S(t) = e^{-2ik_0 r_2}e^{-i\alpha t'^2}e^{i\alpha\tau_0^2}e^{2i\alpha(t'-\tau_0)}\chi(t'-\tau_0). \qquad \text{(A2)}$$

If we set $t'=(1+\zeta)t$ (i.e., the correctly resampled signal), we see that the only difference between (A1) and (A2) is a phase factor $\exp[-i\beta t2(1+\zeta)]$ which can be removed after range compression by post-multiplying the signal.

Notice that, in terms of computation, the chirp scaling algorithm does not increase the number of operations during range compression: it merely changes the reference function, which involves no additional computation. The additional computation occurs in the pre- and post-multiplication of the signal by the appropriate chirp functions. This involves merely N complex multiplications, where N is the number of signal samples, while the range compression involves two $5N\log N$ Fourier transforms and N complex multiplications, so that the resampling is computationally cheap compared to the range compression.

APPENDIX B

Given maximum likelihood estimation, the interferometric phase standard deviation, σ_Φ, is given by

$$\sigma_\Phi = \frac{1}{\sqrt{2N}}\frac{\sqrt{1-\gamma^2}}{\gamma}, \qquad \text{(B1)}$$

where γ is the correlation coefficient between the two interferometric channels:

$$\gamma = \frac{\left| < v^{(1)} v^{(2)*} > \right|}{\sqrt{< v^{(1)} v^{(1)*} > < v^{(2)} v^{(2)*} >}},$$

where the brackets denotes ensemble averaging over speckle realizations. The random height error is due to errors in the estimation of interferometric phase, and is given by [6]

$$\delta h = \frac{r_0 \tan\theta_0}{kB} \sigma_\Phi,$$

where r_0 is the range from the platform to the surface, θ_0 is the look angle, k is the electromagnetic wavenumber, and B is the length of the interferometric baseline.

Equation (B1) shows that the phase standard deviation can be predicted if the correlation coefficient can be modeled. The return signals after range compression co-registration can be modeled as

$$v^{(1)}(t) = A \int \chi_r(t - \frac{2r_1}{c} - \Delta) G(\phi) s(r,\phi) e^{-2ikr_1} dS + n_1$$

$$v^{(2)}(t) = A \int \chi_r(t - \frac{2r_2}{c} - \Delta) G(\phi) s(r',\phi) e^{-2ikr_2} dS + n_2$$

where A is a constant which depends weakly on range; Δ is a delay introduced to co-register the two channels; χ_r is the system range point target response; ϕ is the azimuth angle coordinate (any point in the surface plane can be defined by its ground range ρ and its azimuth angle ϕ); $G(\phi)$ is the system antenna pattern, which is assumed to be much broader in the range direction than the system range resolution, so that only its azimuth variation must be included; r_1 and r_2 represent the range from the reference and secondary antennas to a point on the surface; n_1 and n_2 represent the thermal noise in channels 1 and 2, respectively, and are assumed to be uncorrelated white noise processes with variance N; and, finally, $s(r',\phi)$ represents the rough surface brightness which is assumed to satisfy

$$\left\langle s(r) s^*(r') \right\rangle = \delta(r - r') \sigma_0 \qquad \text{(B2)}$$

where σ_0 is the normalized radar cross section. Equation (B2) is consistent with the deep phase approximation in rough surface scattering [7], which applies when the surface root mean squared roughness is large compared to the wavelength. That approximation is valid for all the systems studied. Notice that we assume that the radar cross section is constant over the radar resolution cell, a good approximation given the relatively high system bandwidth.

To study the effects of the spectral shift algorithm, we introduce the Fourier transform of the range point target response,

$$\chi(t) = \frac{1}{2\pi} \int d\omega e^{i\omega t} W(\omega)$$

and rewrite the equations for the return signal (neglecting for the moment the thermal noise contributions) to obtain

$$v^{(1)}(t) = A \frac{1}{2\pi} \int d\omega e^{i\omega(t-\Delta)} W(\omega) \int dS e^{-2i\omega r_1/c} G(\phi) s(r,\phi) e^{-2ikr_1}$$

$$v^{(2)}(t) = A \frac{1}{2\pi} \int d\omega e^{i\omega(t+\Delta)} W(\omega) \int dS e^{-2i\omega r_2/c} G(\phi) s(r,\phi) e^{-2ikr_2}.$$

The first step of the wavenumber shift algorithm starts by multiplying both of the interferometric signals in the time domain by a phase factor equivalent to the interferometric phase relative to a reference track. Over a localized region, this is equivalent to multiplying by a constant phase factor, and one which varies linearly in time. For our purposes, we will neglect the constant phase term and assume that the first signal is multiplied by a phase factor exp[iwt], while the second is multiplied by the complex conjugate. The result of multiplying by a phase ramp in the time domain will be to shift the spectrum in the frequency domain. We will choose w to maximize the spectral overlap of wavenumber components over the pixel. After shifting the spectra, both signal are low-passed filter with an FIR filter whose frequency response we will denote by $H(\omega)$. The filter characteristics will be chosen below to reduce the noise introduced by the frequency shift.

After both of these operations, the return signals can be written as

$$v^{(1)}(t) = A \frac{1}{2\pi} \int d\omega e^{i\omega(t-\Delta)} W(\omega - w) H(\omega) \int dS e^{-2i(\omega - w) r_1/c} G(\phi) s(r,\phi) e^{-2ikr_1},$$

$$v^{(2)}(t) = A \frac{1}{2\pi} \int d\omega e^{i\omega(t+\Delta)} W(\omega + w) H(\omega) \int dS e^{-2i(\omega + w) r_2/c} G(\phi) s(r,\phi) e^{-2ikr_2}.$$

In order to calculate the interferometric correlation, one must evaluate the expectation value of the channel cross-product:

$$\left\langle v^{(1)}(t)v^{(2)*}(t)\right\rangle = |A|^2\left(\frac{1}{2\pi}\right)^2 \int d\omega_1 \int d\omega_2 e^{i(\omega_1-\omega_2)t} e^{i(\omega_1+\omega_2)\Delta}$$

$$W(\omega_1 - w)W^*(\omega_2 + w)H(\omega_1)H^*(\omega_2)F(\omega_1,\omega_2),$$

where the last function is defined as

$$F(\omega_1,\omega_2) = \sigma_0 \int dS e^{-2i(k_1 r_1 - k_2 r_2)} e^{2i\omega(r_1+r_2)/c} G^2(\phi),$$

and,

$$k_i \equiv k + \omega_i / c.$$

Notice that (B2) is used to reduce the double spatial integral to a single integral.

To proceed further, we notice that we can approximate

$$\begin{aligned} r_1 - r_2 &\approx B[-\sin\theta + \sin\theta(1-\cos\phi)] \\ &\approx B\left[-\sin\theta + \sin\theta\frac{\phi^2}{2}\right], \end{aligned}$$

where we have made use of the fact that the azimuth beamwidth of a typical system is much smaller than one. Expanding about r_0 and θ_0=arccos(H/r_0), this can be further approximated as

$$r_1 - r_2 \approx B\left[-\sin\theta_0 + \sin\theta_0\frac{\phi^2}{2} - \cos^2\theta_0\frac{\delta\rho}{r_0}\right],$$

where

$$\delta\rho = \delta r / \sin\theta_0$$

is the deviation in ground range of the surface point from r_0, and terms of order $(R/(\sin\theta_0 r_0))^2$, where R is the system range resolution, have been neglected.

After making the previous approximation and assuming that we are dealing with a narrow-band system so that , one can evaluate the integral to obtain

$$\begin{aligned} F(\overline{\omega},\Delta\omega) = &\frac{\rho_0\sigma_0}{2\sin\theta_0} e^{2ikB\sin\theta_0} e^{2i\overline{\omega}/cB\sin\theta_0} e^{-2i\Delta\omega r_0/c} e^{4i\omega r_0/c} \\ &c\pi\delta\left(\Delta\omega - 2w - \frac{ckB\cos\theta_0}{r_0\tan\theta_0}\right) \\ &\int d\phi e^{-ikB\sin\theta_0\phi^2} G^2(\phi) \end{aligned}$$

where $\Delta\omega=\omega_1-\omega_2$, and.

$$\overline{\omega} = (\omega_1 + \omega_2)/2$$

Notice that if one chooses the spectral shift

$$\omega = -\frac{c}{2}\frac{kB\cos\theta_0}{r_0\tan\theta_0}$$

the phase is constant over the range resolution cell, for a given azimuth, and it is not hard to convince ones self that the is just the shift in frequency required by geometry so that the projected wavenumber on the ground is the same for both channels. After making this choice for the spectral shift one has that the cross-channel product expectation function can be written as

$$\begin{aligned} \left\langle v^{(1)}(t)v^{(2)*}(t)\right\rangle = &|A|^2 \frac{1}{2\pi}\frac{\rho_0\sigma_0}{2\sin\theta_0} e^{2ikB\sin\theta_0} e^{4i\omega r_0/c} \cdot \\ &\int d\omega e^{2i\omega(-B\sin\theta_0/c-\Delta)} W(\omega - w)W^*(\omega + w)\,|H(\omega)|^2 \cdot \\ &\int d\phi e^{-ikB\sin\theta_0\phi^2} G^2(\phi). \end{aligned}$$

Notice that if the co-registration delay Δ is chosen appropriately, the phase term disappears in the first integral. Furthermore, if one chooses $H(\omega)$ to be centered at zero frequency and with a spectral width of Δf-□/π, where Δf is the bandwidth of W, then only the parts of the signal which correlate on the ground contribute to the return, and no additional noise is brought in due to the spectral shift.

Using the previous results, we obtain the following expression for the complex correlation coefficient

$$\frac{\left|\left\langle v^{(1)}v^{(2)*}\right\rangle\right|}{\sqrt{\left\langle v^{(1)}v^{(1)*}\right\rangle\left\langle v^{(2)}v^{(2)*}\right\rangle}} = \gamma_\phi\gamma_N = \gamma$$

where the angular (γ_ϕ), and noise (γ_N) correlation factors are given by

$$\gamma_\phi = \frac{\int_{-\pi}^{\pi} d\phi e^{-ikB\sin(\theta_0)\phi^2/2} G^2(\phi)}{\int d\phi G^2(\phi)}$$

and

$$\gamma_N = \frac{1}{1 + SNR^{-1}},$$

respectively, where SNR is the system signal-to-noise ratio.

The result obtained for the correlation function share the angular and noise correlation functions with the results previously presented in [1], but the introduction of co-

registration and spectral domain shifts have done away with the misregistration and geometric decorrelation terms. The noise decorrelation term (γ_N) is common to the cross-correlation of any two signals with additive uncorrelated white noise. The fact that the angular correlation term cannot be made to disappear like the geometric correlation term is due to the fact that iso-phase difference contours are hyperbolas, whereas iso-range contours are circles, so that the projected wavelengths can only be made to coincide along one given azimuth direction

ACKNOWLEDGEMENT

This work was performed at the Jet Propulsion Laboratory, California Institute of Technology, under contract with the National Aeronautics and Space Administration (NASA). The authors wish to acknowledge Steve White, Jason Schmidt, David Messner, Gary Heinemann, and the other members of the AEC-Able antenna prototyping team for their excellent work on the deployable antenna and feed structures.

REFERENCES

[1] E. Rodriguez, B.D. Pollard, and J.M. Martin, "Wide swath ocean altimetry using radar interferometry," *IEEE Trans. Geoscience and Remote Sensing*, in press.

[2] S. Datthanasombat and A. Prata, Jr., "Spiral Microstrip Patch Elements for reflectarrays," *2001 IEEE Antennas and Propagation Symposium Proceedings*, July 8-13, 2001.

[3] L. Rabiner, R. Schaffer, and C. Rader, "The chirp-z transform and its applications,", *Bell Syst. Tech. J.*, vol 48, 1249-1292, 1969.

[4] R.K. Raney, H. Runge, R. Bamler, I. Cumming, and F. Wong, "Precision SAR processing using chirp scaling," *IEEE Trans. Geoscience and Remote Sensing*, vol 32, pp 786-799, 1994.

[5] F. Gatelli, A. Monte-Guarniery, F. Parizzi, P. Pasquali, C. Parti, and F. Rocca, "The wavenumber shift in SAR interferometry," *IEEE Trans. Geoscience and Remote Sensing*, vol. 32, no. 4, 855-865, 1994.

[6] E. Rodríguez and J.M. Martin, "Theory and design of interferometric synthetic aperture radars", *IEE Proceedings-F Radar and Signal Processing*, vol, 139, no. 2, pp. 147-159, 1992.

[7] L. Tsang, J.A. Kong, and R.T. Shin, *Theory of Microwave Remote Sensing*, Wiley-Interscience, New York, 1985